Chinese Chemical Letters 34 (2023) 107551

Contents lists available at ScienceDirect

Chinese Chemical Letters

journal homepage: www.elsevier.com/locate/cclet

Pressure-stabilized hexagonal perovskite-related isolated tetrahedral anion silicate $La_6Sr_3Si_6O_{24}$

Jie Feng[a,1], Lei Zhao[a,1], Wenda Zhang[a], Cheng Li[b], Congling Yin[a,*], Xiaojun Kuang[a,c,*]

[a] Guangxi Key Laboratory of Optic and Electronic Materials and Devices, MOE Key Laboratory of New Processing Technology for Nonferrous Metals and Materials, College of Materials Science and Engineering, Guilin University of Technology, Guilin 541004, China
[b] Neutron Scattering Division, Oka Ridge National Laboratory, Oak Ridge 37831, United States
[c] Guangxi Key Laboratory of Electrochemical and Magnetochemical Functional Materials, College of Chemistry and Bioengineering, Guilin University of Technology, Guilin 541004, China

ARTICLE INFO

Article history:
Received 27 March 2022
Revised 8 May 2022
Accepted 20 May 2022
Available online 23 May 2022

Keywords:
High pressure
Hexagonal perovskite
Isolated tetrahedral anion
Silicate
Ionic conductors

ABSTRACT

The discovery of new perovskite compounds under high pressure mainly focuses on the ABO_3 compositions and the compositions highly deviated from ABO_3 are less explored. Here we demonstrate that the $La_6Sr_3Si_6O_{24}$ silicate composition can be stabilized as a hexagonal perovskite-related structure with isolated tetrahedra anions under high pressure of 6 GPa. The compound adopts 9-layer shifted hexagonal perovskite-like structure with both B-cation and oxygen deficiencies and contains pseudo-cubic (c') $(La/Sr)O_2$ layers and hexagonal (h) $(La/Sr)O_3$ layers stacked according to $(c'hh)_3$ sequence. This structure features both B-cation vacancy ordering between the two consecutive hexagonal layers and oxygen vacancy ordering in c'-$(La/Sr)O_2$ layers, resulting in isolated tetrahedral SiO_4 anions and ionic conduction behavior. This work demonstrates the practicability of accessing new perovskite-related functional materials from the compositions highly deviated from ABO_3 under high pressure.

Silicates are known for their natural abundance and are thus widely used in domestic ceramics, glassware, refractories, and building and construction materials [1,2]. Apart from these applications as structural materials, silicates also display interesting functional properties including ferroelectricity [3], nonlinear optical effects [4], luminescence host [5], and ionic conduction [6]. With a variety of chemical composition and structural variations, silicates have the tetrahedral SiO_4^{4-} anion with relative rigidity and strong covalent interactions as the basic structural feature under ambient pressure (AP). The SiO_4^{4-} anions could be isolated [7], or connected into small polymers [8,9], one-dimensional (1D) chains [10], two-dimensional (2D) layers [11], and three-dimensional (3D) framework [12] *via* apex-oxygen sharing, hosting a great variety of metal cations in the resulted voids to compensate the charge.

The ionic metal oxide usually adopts a close packing arrangement of oxygen (and large-size cations) with the metal cations filling in the resulted voids with oxygen coordination number (CN) $\geq$ 6, typically BO_6 octahedron and AO_{12} truncated octahedron in ABO_3 perovskites [13]. In contrast to the ionic metal oxide case, the oxygen ions in the silicates are loosely stacked to satisfy the tetrahedral coordination requirement of Si^{4+}, leading to low space utilization and small CN for the metal cations. For example, typical sodium silicates Na_2SiO_3 [14] and α-$Na_2Si_2O_5$ [15] have 5-coordinated Na^+ cations, while the other ternary ionic metal oxides normally have 6-12 coordinated environments for Na^+, such as those in $NaMnO_2$ [16] and $NaNbO_3$ [17].

Applying high pressures would alter the loosely anionic stacking of the silicates and lead to structural modifications. For example, the stable phase of $MgSiO_3$ enstatite [18] at ambient conditions contains alternative layers of MgO_6 octahedron and SiO_4 tetrahedra (Fig. S1a in Supporting information), which would transform into $MgSiO_3$ ilmenite (Fig. S1b in Supporting information) with SiO_6 octahedral layers at 20-24 GPa (1373-2273 K) [19,20]. Further increasing pressure above 23 GPa (T > 1473 K) leads to the stabilization of $MgSiO_3$ perovskite (Fig. S1c in Supporting information) [21,22], which would convert into the post-perovskite $CaIrO_3$ structure with edge-sharing SiO_6 octahedral chains at pressures > 125 GPa (T > 2500 K) (Fig. S1d in Supporting information) [23]. Due to the different initial size contrast between the ions and atomic compressibility of elements, the structural variation with pressure are different when the cations are changed, as shown by that $CaSiO_3$ parawollastonite [10] with 1D SiO_3^{2-} chains (Fig. S1e in Supporting information) can also

* Corresponding authors.
E-mail addresses: congling.yin@glut.edu.cn (C. Yin), kuangxj@glut.edu.cn (X. Kuang).
[1] These authors contributed equally to this work.

https://doi.org/10.1016/j.cclet.2022.05.065
1001-8417/

transform into perovskite at 14-16 GPa [24] and $SrSiO_3$, which are composed of alternating layers of $Si_3O_9^{6-}$ rings and layers of 8-coordinated Sr atoms (Fig. S1f in Supporting information) [9], convert into hexagonal perovskite at 20 GPa then cubic perovskite at 32 GPa [25,26]. Generally, the non-perovskite silicates $MSiO_3$ with small B-site cations would adopt perovskite structure at certain pressure as those observed in other ABO_3 systems with small A-site cations [27].

Recently lanthanum silicates have been explored extensively under AP for their interesting properties on luminescence and ionic conduction, *e.g.*, La_2SiO_5 [28], $La_{9.33+x}(SiO_4)_6O_{2+1.5x}$ ($x = 0$-0.67) [29,30] and $La_2Si_2O_7$ [8,31,32]. La_2SiO_5 features an isolated SiO_4 tetrahedron and oxosilicate nature with some oxygen anions only bonding to La cations (Fig. S1g in Supporting information). While $La_2Si_2O_7$ has four polymorphs: the *A*-type (tetragonal, $P4_1$), *G*-type (monoclinic, $P2_1/c$), and *H*-type (triclinic, $P\bar{1}$) structures containing diorthosilicate $Si_2O_7^{6-}$ anions built up of two corner-linked SiO_4 tetrahedra (Fig. S1h in Supporting information) [8,31], the *I*-type containing a hoof-shaped catena-tetrasilicate $Si_4O_{13}^{10-}$ ions and two orthosilicates SiO_4^{4-} ions per formula unit (Fig. S1i in Supporting information) [32]. Among these four polymorphs of $La_2Si_2O_7$, the tetragonal *A*-type phase is thermodynamically stable at room temperature, while the other phases are metastable [8]. The $La_{9.33+x}(SiO_4)_6O_{2+1.5x}$ ($x = 0$-0.67) compositions, which lie between La_2SiO_5 and $La_2Si_2O_7$, adopt apatite structure, which is built up of isolated SiO_4 tetrahedron with La^{3+} cations located in the 7- and 9-coordinated sites and the remaining O^{2-} anions occupying channel along the *c*-axis (Fig. S1j in Supporting information). The $La_{9.33+x}(SiO_4)_6O_{2+1.5x}$ apatite features extra oxygen atoms or La vacancies, which prompt oxide conduction through an interstitial mechanism [29,33]. Replacing La partially with Sr in $La_{9.33+x}(SiO_4)_6O_{2+1.5x}$ leads to a stoichiometric apatite of $La_8Sr_2(SiO_4)_6O_2$ with the oxide ion mobility reduced significantly [34]. Compared with the alkaline earth silicates, the lanthanum-based silicates received less attention on the pressure-induced structural evolution. A high-pressure (HP) lanthanum silicate has been reported as $La_4Si_3O_{12}$ with a monoclinic cell twenty years ago. However, the crystal structure of the HP silicate $La_4Si_3O_{12}$ is problematic and contains only rudimentary information [35,36].

For the non-perovskite ABO_3 compositions under AP, it is relatively easy to predicate the HP transformation to perovskite structure although there could be intermediate polymorphs before reaching the dense perovskite structure. While for the compositions highly deviated from ABO_3, the prediction of transformation to perovskite structure is not straightforward under high pressure. However, the defected perovskite structures could be expected if these compositions can form perovskite-related structures under high pressure, which may provide an effective strategy for new functional materials. So far there is little attention to HP preparation of the defected perovskite-related structures from the compositions highly deviated from ABO_3 [37].

To address the possibility of perovskite-related structure formation in the compositions highly deviated from ABO_3, we have been investigating the structural evolution of the less explored lanthanum silicates under high pressure. Herein we report that $La_6Sr_3Si_6O_{24}$ composition, which forms a mixed apatite and $SrSiO_3$ phase at ambient pressure, transformed to a highly defected hexagonal perovskite-related structure with both B-cation and oxygen deficiencies under high pressure around 6 GPa. This hexagonal perovskite-related structure features B-cation and oxygen vacancy ordering, leading to isolated tetrahedral SiO_4 units, and ionic-conducting behavior.

The synthesis attempt at the composition of $La_6Sr_3Si_6O_{24}$ at 1473 K and AP leads to a mixed phase of $La_8Sr_2Si_6O_{26}$ apatite [34] and $SrSiO_3$ [9], as evidenced by the Rietveld plot shown in Fig. S2a (Supporting information). The coexistence of two phases

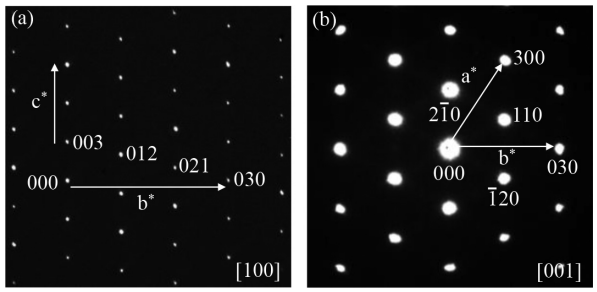

Fig. 1. Electron diffraction patterns of $La_6Sr_3Si_6O_{24}$ recorded along the (a) [100] and (b) [001] directions.

with significant compositional contrast is directly observed with SEM images from backscattered electrons and EDS elemental mapping, as shown in Fig. S3 (Supporting information). An unknown HP phase started to appear on the XRD data of $La_6Sr_3Si_6O_{24}$ (Fig. S2b in Supporting information) as the applied pressure reached 3 GPa and above, and its phase content increased with pressure. At pressure above 6 GPa, the reflections of the AP phases disappeared, and the HP phase was isolated as a single-phase material. The EDS elemental analysis of the HP material gives an average cation ratio of $La_{6.2(4)}Sr_3Si_{6.1(2)}$ across the sample (Figs. S4 and S5 in Supporting information), which reasonably keeps with the nominal stoichiometric composition of $La_6Si_3Si_6O_{24}$.

The XRD pattern of HP $La_6Sr_3Si_6O_{24}$ sample can be indexed into a hexagonal cell with lattice parameters of $a = 5.4326(8)$ Å and $c = 19.6174(3)$ Å, showing the reflection conditions: $hkil$: $-h+k+l = 3n$ and $000l$: $l = 3n$, which suggest a rhombohedral hexagonal lattice type and possible space groups of *R*3, $R\bar{3}$, *R*32, *R*3m, and $R\bar{3}m$. Figs. 1a and b show the SAED patterns of the $La_6Sr_3Si_6O_{24}$ sample collected along the [100] and [001] directions, respectively. No superstructure weak reflections were observed and all the reflections are compatible with the hexagonal cells and the possible space groups above. Therefore, the space group $R\bar{3}m$ with the highest symmetry was chosen in the following structure determination.

The *ab initio* structure solution of $La_6Sr_3Si_6O_{24}$ was performed based on the XRD data in the space group $R\bar{3}m$ by the direct method using EXPO2014 [38,39], in which the initial positions of heavier lanthanum and strontium atoms can be directly determined. Subsequently, silicon and oxygen positions were obtained by the difference Fourier analysis. Rietveld refinements of lattice parameters, atomic positions, and isotropic displacement parameters (B_{iso}) were carried out simultaneously against the XRD and NPD data. The mixed occupancies of La and Sr were identified and refined on the 10 and 12-fold coordinated sites. The initial refinement found a relatively large atomic displacement parameter on the ideal O1 site *6c* (0, 0, *z*). Therefore, a split general position 18*h* with a fractional occupancy of one third was adopted for the O1 site in the following refinements. The final refinement converged to reliability factors R_{wp} of ~4.62% and 6.85% for XRD and NPD data as shown in Figs. 2a and b, respectively, and the final refined atomic coordinates are given in Table 1.

The crystal structure of HP $La_6Sr_3Si_6O_{24}$ can be described as both oxygen and B-cation deficient hexagonal perovskite (Fig. 3a), in comparison with its corresponding 9-layer B-site deficient shifted hexagonal perovskite $A_3B_2O_9$ [40] with the similar stacking sequence of $(chh)_3$ (*c* and *h* denote cubic and hexagonal stacking of close-packed AO_3 layers, respectively) and oxygen vacancies filled (Fig. 3b). The stacking sequence of HP $La_6Sr_3Si_6O_{24}$ is $(c'hh)_3$, where c' denotes an oxygen-deficient $(La/Sr)O_2$ pseudo-cubic-stacking layer (Fig. 3c), and *h* denotes a close-packed $(La/Sr)O_3$ layer (Fig. 3d). Due to the formation of the $(La/Sr)O_2$ oxygen-

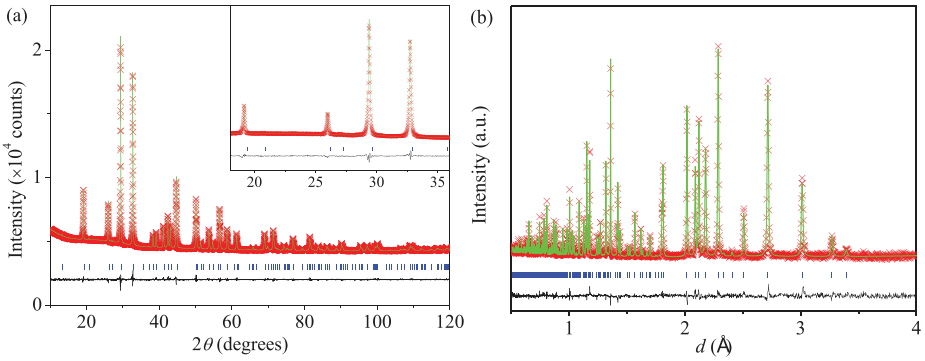

Fig. 2. Observed (red crosses), calculated (green line) and difference plots (black line) for the structure refinement of HP $La_6Sr_3Si_6O_{24}$ against (a) XRD and (b) NPD data. The R_{wp} (R_p) factors are ~6.17% (~7.29%) and ~4.62% (~3.49%) for NPD and XRD data, respectively. The inset in (a) enlarges the reflections in the 2θ range from 18° to 36°.

Table 1
Final refined structural parameters for $La_6Sr_3Si_6O_{24}$*.

Atom	Site	x	y	z	Occupancy	B_{eq} (Å^2)	BVS
La1/Sr1	3*a*	0	0	0	0.91/0.09(1)	1.37(2)	2.83/2.45
La2/Sr2	6*c*	0	0	0.7951(4)	0.55/0.45(4)	0.69(1)	2.76/2.38
Si	6*c*	0	0	0.5938(7)	1	0.97(6)	4.00
O1	18*h*	−0.3099(3)	0.3099(3)	0.6773(7)	1/3	0.80(3)	
O2	18*h*	0.4968(9)	0.5032 (9)	0.2331(4)	1	0.79(8)	

*$a = 5.4384(2)$ Å, $c = 19.6383(1)$ Å, space group: $R\bar{3}m$, $Z = 1$.

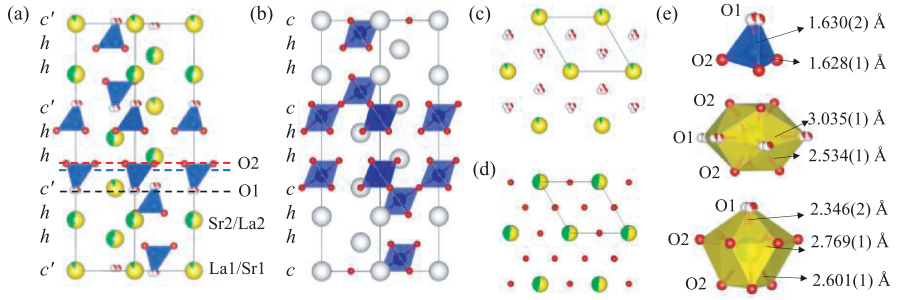

Fig. 3. The structure viewed along the [110] direction for (a) $La_6Sr_3Si_6O_{24}$ oxygen-deficient perovskite and (b) its corresponding 9-layer shifted hexagonal perovskite $A_3B_2O_9$ without oxygen vacancy. (c) and (d) show the oxygen-deficient *c*′-(La/Sr)O_2 layer and the close-packed *h*-(La/Sr)O_3 layer in $La_6Sr_3Si_6O_{24}$, as marked with dashed black and red lines in (a), respectively. (e) The coordination environments of Si, La1/Sr1, and Sr2/La2 from the top to bottom.

deficient layer and oxygen vacancy ordering, the 6-coordinated octahedral site formed between the neighboring *c*-layer and *h*-layer in $A_3B_2O_9$ perovskite turned into the 4-coordinated tetrahedral site, which is occupied by the perovskite B-site cations (here, Si^{4+} cation). The octahedral sites between the two adjacent *h* layers are vacant in $La_6Sr_3Si_6O_{24}$, leading to a layered arrangement of B-site Si^{4+} cations tetrahedra and octahedral vacancies. The SiO_4 tetrahedron has two sets of Si-O bonds with essentially identical lengths of ~1.63 Å (Fig. 3e top), which keeps with its average value of ~1.62 Å in the literature [1].

Interestingly, the A-site cations La and Sr in $La_6Sr_3Si_6O_{24}$ are not randomly distributed over the 3*a* and 6*c* sites in the *c*′ and *h* layers although they have a similar ionic radius of 1.44 Å and 1.36 Å (with CN = 12), respectively [41]. This partial site occupancy leads to relatively low bond valence sum (BVS) values of La^{3+} (2.83 and 2.76) and high BVS values for Sr^{2+} (2.45 and 2.38) on both sites, similar to those in $La_8Sr_2Si_6O_{26}$ [34]. The La atoms prefer to occupy the 3*a* site in the oxygen-deficient AO_2 layer, forming a 12-coordinated environment (Fig. 3e middle), while the Sr cations concentrate in the close-packed AO_3 layer with CN = 10 (Fig. 3e bottom). This site selectivity is probably driven by the charge difference rather than the size difference since the slightly larger Sr^{2+} cation usually prefers a higher CN than La^{3+} ion. As shown in Fig. 3a, the Si^{4+} cationic layer (dashed blue line) is much closer to the *h*-AO_3 layer (red dashed line) than the *c*′-AO_2 layer (dashed black line), and has dominant electrostatic interaction with the former. To balance the positive charge of the adjacent Si^{4+} layer, the *h*-AO_3 layers prefer to accommodate nearly all available Sr^{2+} than La^{3+} ions to carry more negative charges.

The thermal stability of $La_6Sr_3Si_6O_{24}$ was investigated by the thermal analysis (Fig. S6a in Supporting information) and temperature varied XRD (Fig. S6b in Supporting information). No phase transition was observed on the *in-situ* XRD data within the 298-1073 K temperature range, while trace amounts of impurity reflections appeared at $T = 1273$ K, indicative of decomposition. A complete decomposition was reached for the sample heated at 1273 K for 12 h (Fig. S6c in Supporting information). The decomposition started below 1173 K, as suggested by the secondary peaks on the XRD plot of the sample annealed at 1173 K for 6 h. No impurity phases were observed for the HP $La_6Sr_3Si_6O_{24}$ compound annealed at 1073 K for 10 h, suggesting its good dynamical stability. The lattice parameters of HP $La_6Sr_3Si_6O_{24}$ phase increase linearly as the temperature increases (Fig. S6d in Supporting information), showing anisotropic thermal expansions of $\alpha_a = 11.7 \times 10^{-6}$ K^{-1} and $\alpha_c = 7.9 \times 10^{-6}$ K^{-1}, keeping with rhombohedral structural anisotropy. This leads to an overall linear volume expan-

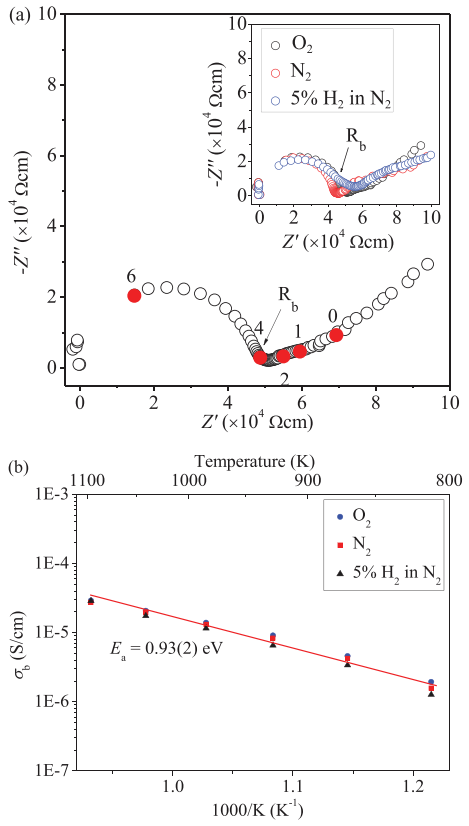

Fig. 4. (a) The 1023 K complex impedance plots for $La_6Sr_3Si_6O_{24}$ pellets measured under O_2 atmosphere in comparison with those in N_2 and 5% H_2 in N_2 atmospheres in the inset. R_b denotes the bulk resistivity and the numbers denote the logarithms of selected frequencies marked by filled symbols. (b) Temperature-dependent bulk conductivities of $La_6Sr_3Si_6O_{24}$ pellets in the O_2, N_2, and 5% H_2 in N_2 atmospheres with activation energy (E_a) labeled.

sion of $\alpha_v = 31.6 \times 10^{-6}$ K^{-1} at the 298-1273 K temperature range.

Generally, the application of high pressure tends to densify the materials by leading to a shorter atomic distance and thus increasing the CN of the cation and anions [42,43]. The denser atomic stacking in the HP $La_6Sr_3Si_6O_{24}$ phase can be understood through the structure comparison with the AP $SrSiO_3$, $La_8Sr_2Si_6O_{26}$ phases, in which although the Si atoms have similar 4-fold coordinations, the La and Sr atoms have different coordination environments. The Sr^{2+} cations are 8-oxygen coordinated in the $SrSiO_3$ phase, in contrast with the 7 and 9-oxygen coordinated La^{3+} and Sr^{2+} ions in the $La_8Sr_2Si_6O_{26}$ apatite. However, the HP $La_6Sr_3Si_6O_{24}$ phase has larger CN for Sr and La than both AP phases, *i.e.,* 12 and 10. Thus, the driving force for the phase reaction of $6SrSiO_3 + 3La_8Sr_2Si_6O_{26} \rightarrow 4La_6Sr_3Si_6O_{26}$ can be related to the increasing of the cationic CN and the more close-packed cations and anions under pressure.

To explore the transport properties of $La_6Sr_3Si_6O_{24}$, AC impedance data was collected on the 1027 K annealed pellet, which has 95.4(1)% of the theoretical density. The samples as-quenched from the HP synthesis have many strain-induced defects and a large proportion of small grains (Fig. S4), which would recrystallize during the measurement, evidenced by the exothermal thermal peak at ~600 K (Fig. S6a) and give history-dependent impedance data. However, the $La_6Sr_3Si_6O_{24}$ sample annealed at 1073 K contains large grains and well-defined grain boundaries (Fig. S5) and gives identical conductivities on heating and cooling.

Fig. 4a shows typical complex impedance plots at 1023 K measured at different atmospheres, which are essentially identical and consist of one symmetric semicircle arc and apparent Warburg-type electrode response tails. The semicircular arc can be modeled with a parallel Resistor-Capacitance (*RC*) circuit: the intercept of the semicircular arc at low frequency is estimated as *R*; the associated *C* value calculated from the equation $2\pi f_{max} RC = 1$ (f_{max} is the frequency corresponding to the maximum imaginary impedance Z''_{max}) is ~4.9 pF/cm. This value is close to that (~5.4 pF/cm) estimated from the maximum imaginary modulus M''_{max} using the equation $\varepsilon_0/(2M''_{max})$ (ε_0 is the capacitance of free space, 8.854×10^{-14} F/cm). This confirms that the semicircular arc can be ascribed to a single bulk component response [44,45]. The electrode responses in the impedance data of $La_6Sr_3Si_6O_{24}$ pellet show large capacitances of ~10^{-8}-10^{-6} F/cm in the 10-0.1 Hz low-frequency region, which is indicative of ionic conduction in $La_6Sr_3Si_6O_{24}$ [45]. Apart from the semicircular-arc bulk response and the inclined-line electrode response, no apparent semicircular arc was observed from the grain boundary response, which however could be disguised between the bulk and electrode responses as indicated by the capacitances around 10^{-11}-10^{-9} F/cm in the 10^4-10^2 Hz frequency range.

Recently the B-cation and oxygen-deficient hexagonal perovskite transitional metal oxides (*e.g.,* $Ba_3WNbO_{8.5}$ [46], $Ba_7Nb_4MoO_{20}$ [47,48], and $Ba_7Y_2Mn_3Ti_2O_{20}$ [49]) have been shown to transport the oxide ions. In these hexagonal perovskites, the oxygen-vacancy ordered *c*'-AO_2 layers could transform to oxygen-vacancy disordered *c*-AO_{3-x} layers thus allowing the oxide ion migration within the oxygen-deficient layer among the sites corresponding to tetrahedral/octahedral units. Here to find out whether the mobile species in $La_6Sr_3Si_6O_{24}$ are oxygen ions, we conducted tests in different atmospheres of oxygen, nitrogen, and 5% H_2 in N_2 and found that the electrode responses are almost independent of the atmosphere (Fig. 4a). This phenonium is unlike the typical behavior of electrode response with the partial oxygen pressure change for the oxide ion conductors with good oxide ion conductivities (*e.g.,* $>10^{-3}$ S/cm) [50,51]. However, for materials having small and constant carrier concentrations which are determined by intrinsic thermal activation rather than extrinsic oxide-ion substitution from the atmosphere, the oxide-ion conductivity could be independent of pO_2 and the inclined electrode response line could be hardly affected by the atmosphere change. Considering low total conductivities within 10^{-6}-10^{-4} S/cm with large activation energy (~0.93 eV), as well as its atmosphere-independent nature (Fig. 4b) although minor *p*-type conduction can be still discerned, such low-level ionic conduction in $La_6Sr_3Si_6O_{24}$ could be still ascribed to the oxygen ions. Such oxide ion conduction could be correlated with the oxygen-vacancy ordered *c*'-AO_2 layers in $La_6Sr_3Si_6O_{24}$, similar to the hexagonal perovskite oxide ion conductors mentioned above. As indicated by the larger atomic displacement parameter compared with the La2/Sr2 atoms, the La1/Sr1 atoms in the oxygen-deficient *c*' layers were also considered to be the likely ions for the migration due to their relatively loose packing nature in the structure. However, as indicated by the SEM-EDS results (Fig. S7 in Supporting information), both surfaces of the pellet adjacent to the negative and positive electrodes, and also the cross-section of the pellet parallel to the current direction, show homogeneous elemental distributions and an identical La:Sr:Si ratio with the nominal value (2:1:1) after direct current (DC) polarization. This observation indicated no apparent La or Sr aggregation near the negative electrode side, thus excluding these cations as the ionic conduction species in the sample.

In summary, the 9-layer B-cation and oxygen-deficient shifted hexagonal perovskite-related structure was stabilized on $La_6Sr_3Si_6O_{24}$ composition under high pressure at 6 GPa. Combined Rietveld refinements of XRD and NPD data indicate B-cation vacancy ordering between two consecutive *h*-$(La/Sr)O_3$ layers and

oxygen vacancy ordering in the c'-(La/Sr)O_2 layers, and stacking order of $(c'hh)_3$ in $La_6Sr_3Si_6O_{24}$. The HP $La_6Sr_3Si_6O_{24}$ features isolated SiO_4 tetrahedral anions between c' and h layers and low-level ionic conduction behavior. The results here indicate that it is practicable to design and synthesize new perovskite-related functional materials from the compositions highly deviated from ABO_3 under high pressure.

Declaration of competing interest

The authors declare no competing financial interests.

Notes

CSD 2160488 contains the supplementary crystallographic data for this paper. The data can be obtained free of charge *via* www.ccdc.cam.ac.uk/data_request/cif, or by emailing data-request@ccdc.cam.ac.uk, or by contacting The Cambridge Crystallographic Data Centre, 12 Union Road, Cambridge CB2 1EZ, U.K.; fax: +44 1223 336033.

Acknowledgments

The authors thank the National Science Foundation of China (Nos. 21875049, 22090043 and 22161014), Guangxi Natural Science Foundation (Nos. 2019GXNSFGA245006, AD19245097 and 2020GXNSFAA297220), and the Foundation of Guilin University of Technology (No. GUTQDJJ2018115) for the financial support. We thank Prof. Yonggang Wang (Center for High Pressure Science & Technology Advanced Research, Beijing) for proving facility in the thermal analysis.

Supplementary materials

Supplementary material associated with this article can be found, in the online version, at doi:10.1016/j.cclet.2022.05.065.

References

[1] F. Liebau, Structural Chemistry of Silicates, Springer, Berlin, Heidelberg, 1985.
[2] D.Y. Pushcharovsky, N.V. Zubkova, I.V. Pekov, Struct. Chem. 27 (2016) 1593–1603.
[3] H. Taniguchi, A. Kuwabara, J. Kim, et al., Angew. Chem. Int. Ed. 52 (2013) 8088–8092.
[4] H.P. Wu, B.B. Zhang, H.W. Yu, et al., Angew. Chem. Int. Ed. 59 (2020) 8922–8926.
[5] A.J. Fernandez-Carrion, M. Allix, M. Ocana, et al., Inorg. Chem. 52 (2013) 13469–13479.
[6] S. Nakayama, M. Sakamoto, J. Eur. Ceram. Soc. 18 (1998) 1413–1418.
[7] J.G. Wang, S.J. Tian, G.B. Li, et al., Mater. Res. Bull. 36 (2001) 1855–1861.
[8] J. Felsche, J. Less-Common Met. 21 (1970) 1–14.
[9] F. Nishi, Acta Crystallogr. C 53 (1997) 534–536.
[10] F.J. Trojer, Z. Kristallogr. 127 (1968) 291–308.
[11] R.M. Douglass, Am. Mineral. 43 (1958) 517–536.
[12] A.E. Lapshin, N.B. Borisova, V.M. Ushakov, et al., Russ. J. Inorg. Chem. 51 (2006) 438–444.
[13] A.S. Bhalla, R.Y. Guo, R. Roy, Mater. Res. Innov. 4 (2000) 3–26.
[14] W.S. Mcdonald, D.W.J. Cruickshank, Acta Cryst. 22 (1967) 37.
[15] A.K. Pant, D.W.J. Cruickshank, Acta Crystallogr. B 24 (1968) 13.
[16] M. Jansen, R. Hoppe, Z. Anorg. Allg. Chem. 399 (1973) 163–169.
[17] C.N.W. Darlington, K.S. Knight, Acta Crystallogr. 55 (1999) 24–30.
[18] N. Morimoto, K. Koto, Z. Kristallogr. 129 (1969) 65–83.
[19] T. Yamanaka, Y. Komatsu, M. Sugahara, et al., Am. Mineral. 90 (2005) 1301–1307.
[20] H. Horiuchi, M. Hirano, E. Ito, et al., Am. Mineral. 67 (1982) 788–793.
[21] Y.B. Wang, F. Guyot, A. Yeganehhaeri, et al., Science 248 (1990) 468–471.
[22] T. Tsuchiya, J. Tsuchiya, K. Umemoto, et al., Earth Planet. Sci. Lett. 224 (2004) 241–248.
[23] M. Murakami, K. Hirose, K. Kawamura, et al., Science 304 (2004) 855–858.
[24] S.H. Shim, T.S. Duffy, G.Y. Shen, J. Geophys. Res. Solid Earth 105 (2000) 25955–25968.
[25] M. Akaogi, H. Kojitani, H. Yusa, et al., Phys. Chem. Miner. 32 (2005) 603–613.
[26] W.S. Xiao, D.Y. Tan, W. Zhou, et al., Am. Mineral. 98 (2013) 2096–2104.
[27] A.A. Belik, W. Yi, J. Phys. Condens. Matter 26 (2014) 163201.
[28] K. Fukuda, T. Iwata, E. Champion, Powder Diffr. 21 (2006) 300–303.
[29] L. Leon-Reina, E.R. Losilla, M. Martinez-Lara, et al., J. Mater. Chem. 14 (2004) 1142–1149.
[30] B. Li, W. Liu, W. Pan, J. Power Sources 195 (2010) 2196–2201.
[31] H. Muller-Bunz, T. Schleid, Z. Anorg. Allg. Chem. 626 (2000) 2549–2556.
[32] H. Muller-Bunz, T. Schleid, Z. Anorg. Allg. Chem. 628 (2002) 564–569.
[33] P.R.Slater Jones, M.S. Islam, Chem. Mater. 20 (2008) 5055–5060.
[34] Y. Masubuchi, M. Higuchi, T. Takeda, Solid State Ionics 177 (2006) 263–268.
[35] X.Y. Liu, M.E. Fleet, J. Phys.-Condens. Matter 14 (2002) 11223–11226.
[36] M.E. Fleet, X.Y. Liu, Am. Mineral. 89 (2004) 396–404.
[37] J.A. Rodgers, A.J. Williams, J.P. Attfield, Z. Naturforsch. B 61 (2006) 1515–1526.
[38] M.Camalli Altomare, C. Cuocci, et al., J. Appl. Crystallogr. 42 (2009) 1197–1202.
[39] C.Cuocci Altomare, C. Giacovazzo, et al., J. Appl. Crystallogr. 46 (2013) 1231–1235.
[40] D. Urushihara, T. Asaka, K. Fukuda, et al., Inorg. Chem. 56 (2017) 13007–13013.
[41] R.D. Shannon, Acta Crystallogr. A 32 (1976) 751–767.
[42] S. Zhao, J.J. Yang, Y.F. Han, et al., Chin. Chem. Lett. 34 (2023) 107355.
[43] Y.F. Han, Y.J. Zeng, M. Hendrickx, et al., J. Am. Chem. Soc. 142 (2020) 7168–7178.
[44] F.D. Morrison, D.C. Sinclair, A.R. West, J. Am. Ceram. Soc. 84 (2001) 531–538.
[45] J. Irvine, D.C. Sinclair, A.R. West, Adv. Mater. 2 (1990) 132–138.
[46] S. Fop, J. Skakle, A.C. Mclaughlin, et al., J. Am. Chem. Soc. 138 (2016) 16764–16769.
[47] S. Fop, K.S. Mccombie, E.J. Wildman, et al., Nat. Mater. 19 (2020) 752–757.
[48] M. Yashima, T. Tsujiguchi, Y. Sakuda, et al., Nat. Commun. 12 (2021) 556.
[49] X.J. Kuang, M. Allix, R.M. Ibberson, et al., Chem. Mater. 19 (2007) 2884–2893.
[50] M. Li, H. Zhang, S.N. Cook, et al., Chem. Mater. 27 (2015) 629–634.
[51] X.Y. Yang, A.J. Fernández-carrióN, J.H. Wang, et al., Nat. Commun. 9 (2018) 4484.